Revealing the residual stress distribution in laser welded Eurofer97 steel by neutron diffraction and Bragg edge imaging

Bin Zhu[a], Nathanael Leung[a], Winfried Kockelmann[b], Saurabh Kabra[b], Andrew J. London[c], Michael Gorley[c], Mark J. Whiting[a], Yiqiang Wang[c,*], Tan Sui[a,*]

[a] School of Mechanical Engineering Sciences, University of Surrey, Guildford, Surrey GU2 7XH, United Kingdom
[b] Science and Technology Facilities Council (STFC) Rutherford Appleton Laboratory, ISIS Facility, Harwell OX11 0QX, United Kingdom
[c] United Kingdom Atomic Energy Authority, Culham Centre for Fusion Energy, Culham Science Centre, Abingdon, Oxon OX14 3DB, United Kingdom

ABSTRACT

Eurofer97 steel is a primary structural material for applications in fusion reactors. Laser welding is a promising technique to join Eurofer97 plasma-facing components and overcome remote handling and maintenance challenges. The interaction of the induced residual stress and the heterogeneous microstructure degrades the mechanical performance of such fusion components. The present study investigates the distribution of residual stress in as-welded and post-heat treated Eurofer97 joints. The mechanistic connections between microstructure, material properties, and residual stress are also studied. Neutron diffraction is used to study the through-thickness residual stress distribution in three directions, and neutron Bragg edge imaging (NBEI) is applied to study the residual strain in high spatial resolution. The microstructures and micro-hardness are characterised by electron backscatter diffraction and nanoindentation, respectively. The M-shaped residual stress distribution through the thickness of the as-welded weldment is observed by neutron diffraction line scans over a region of 1.41×10 mm^2. These profiles are cross-validated over a larger area ($\sim56 \times 40$ mm^2) with the higher spatial resolution by NBEI. The micro-hardness value in the fusion zone of the as-welded sample almost doubles from 2.75 ± 0.09 GPa to 5.06 ± 0.29 GPa due to a combination of residual stress and cooling-induced martensite. Conventional post weld heat treatment (PWHT) is shown to release $\sim 90\%$ of the residual stress but not fully restore the microstructure. By comparing its hardness with that of stress-free samples, it is found that the microstructure is the primary contribution to the hardening. This study provides insight into the prediction of structural integrity for critical structural components of fusion reactors.

© 2022 Published by Elsevier Ltd on behalf of The editorial office of Journal of Materials Science & Technology.

1. Introduction

Nuclear fusion is a potential substitute source of electricity production and could address the current dependence on fossil fuels, and thus, the well-known environmental issues resulting from carbon emissions. A series of fusion tokamaks have been developed, from the Joint European Torus (JET), the International Thermonuclear Experimental Reactor (ITER) to the DEMOnstration power plant (DEMO). Reduced-activation ferritic/martensitic (RAFM) steels are modified to maintain the high Cr Grade 91 steel's high temperature mechanical, thermal and physical properties by replacing Mo with lower activation elements like W and Ta [1–4]. Eurofer97, one of the RAFM steels, is the European baseline struc-

tural material for the in-vessel components (e.g. pipes, breeding blanket and divertor cassette) for the EU-DEMO [5–7]. The design of these in-vessel structures imposes inherent assembly difficulties because of the internal grid structure and the meandering helium or water coolant circulation channels in the blanket plates [8]. The pipe connections of these breeding blanket components require quick, reliable welding and joining techniques to maintain structural integrity. Because of both radiation levels and limited access, the joining and cutting processes must be completed by remote in-bore tools for fabrication and maintenance [9].

Laser welding performed by a robotic device is one of the most promising techniques, which could serve both cutting and welding operations. Compared with other welding techniques, laser welding gives rise to less distortion, enables full penetration of single-pass welds in thick sections, and has low heat input, leading to a narrow heat affected zone (HAZ). Previous studies have demonstrated the feasibility of remote laser tools to manufacture and

maintain the in-vessel components in fusion plants by laser welding [9–11]. This rapid welding process does, however, induce significant residual stresses of up to approximately 800 MPa inside the welded steel, which is predominantly attributed to the non-uniform thermal expansion and contraction and the martensitic phase transformation during the welding cycle [12–14]. It is well-known that residual stress associated with complex microstructures affects the integrity, mechanical properties, and microstructure of laser-welded Eurofer97 [3,8,9,11,15,16]. For example, the elevated in-service temperatures release the residual stress, which aggravates the creep cracking initiation under the high tensile residual stress condition [17,18], whereas the compressive residual stress resists crack growth but leads to buckling [19]. Therefore, evaluating the residual stress and exploring the degradation of mechanical properties and their interaction with microstructure are crucial for determining reliability and developing predictive tools for the in-vessel components of DEMO.

Neutron-based techniques have been used effectively to measure the residual lattice strain in welds non-destructively due to their high penetration and volume-averaged bulk information contents [20]. The time-of-flight (TOF) method is beneficial as several peaks, each corresponding to an {hkl} lattice plane, are measured simultaneously [21]. Neutron diffraction can be used to determine the through-thickness residual stress in three dimensions throughout a sample [22]. The spatial resolution measured by neutron diffraction is, however, limited by the gauge volume (typically from 1 mm^3 to 9 mm^3) [23]. Some attempt was made to study the residual stress by using {211} lattice planes at a depth of 1.25 mm below the surface on the laser-welded Eurofer97 by neutron diffraction [12,24], but the chemical and microstructural changes in the HAZ were not considered in selecting stress-free (d_0) reference lattice spacing. Additionally, the through-thickness residual stress distribution and high-resolution (HR-) strain field across the weldment was not provided.

Neutron Bragg edge imaging (NBEI) is a relatively new strain measurement technique that follows principles similar to the TOF method, which can provide a high spatial resolution strain projection averaged over neutron path lengths via a pixelated detector in a single neutron beam exposure [25]. Further processes of projection at different angles can achieve strain tomography reconstruction [26]. Due to the recent development of a micro-channel plate (MCP) neutron imaging detector, the NBEI technique provides residual strain maps in a large area (28 × 28 mm^2) with a spatial resolution of 200 μm [27,28]. Bragg edge broadening was also used to analyse the quantity of martensite in the quenched steel, which is related to its hardness [29]. The residual strain measurement, obtained by NBEI, was used to map the residual strain distribution in the teeth and core position of the heat-treated gears and the 316L stainless steel fabricated by additive manufacture [30,31]. However, using a constant reference lattice spacing from theoretical lattice parameters and annealed samples in these studies gives rise to uncertainties due to local variations in microstructure and composition.

In summary, the mechanistic connections between microstructure, residual stress, and micro-hardness of laser-welded Eurofer97 steel have not been established due to (i) uncertainty of the residual stress in laser-welded Eurofer97 steels, and (ii) the unknown relative contributions of residual stress and microstructure to the material properties. The motivation for this study was to quantitatively evaluate the residual stress in laser-welded Eurofer97 steel by using neutron-based techniques. Such techniques provided a deeper insight into the residual stress distribution in the material, with the NBEI technique offering a better description of the strain fields via the HR-maps. In addition, the micro-hardness and microstructure were characterised to establish their interdependence. Post weld heat treatment (PWHT) was performed to relieve the residual stress, and the micro-hardness of the PWHT sample was measured. This information enabled an understanding of how the micro-hardness altered via the reduction of the residual stress, providing insights into predicting the mechanical performance of the components under the working circumstances. Such an understanding of the relationship between residual stress, microstructure, and mechanical properties enables the manufacture of joints with improved service life.

2. Materials and methods

2.1. Materials

The Eurofer97 steel was made by Böhler Austria GmbH with a composition of Fe-0.11C-8.82Cr-1.08W-0.13Ta-0.48Mn-0.2 V (in wt.%) was used in the present investigation. The detailed fabrication, rolling processes and heat treatment of Eurofer97 steel were described in a previous study [32]. The as-welded plate was butt welded perpendicular to the rolling direction by two as-received Eurofer97 steel plates, with dimensions 150 × 75 × 6 mm^3. A 5 kW Yb-fibre laser source with a welding speed of 1.2 m/min was employed for the single laser welding by The Welding Institute(TWI), which enabled a fully penetrating narrow bead with limited spatter and a slightly concave shape. As shown in Fig. 1(a), two as-welded samples (#1 and #3) approximately ∼60 × 40 × 6 mm^3 in size and two comb-shaped stress-free samples (#2 and #4) approximately ∼30 × 6 × 6 mm^3 in size were cut from the as-welded plate by electrical discharge machining (EDM). To understand the effect of a conventional PWHT on residual stress relaxation and re-distribution, samples #3 and #4 were annealed at 760 °C for 1.5 h in a vacuum, followed by furnace cooling.

Samples #1 and #3 were cut to a suitable dimension (25 × 6 × 6 mm^3) for microstructure and micro-hardness characterisation after neutron diffraction and NBEI experiments. A surface preparation, including mechanical polishing with a final vibration polishing step and etching with Vilella's reagent was performed. Reflected light microscopy was used to distinguish the dimension of FZ and HAZ regions of the as-welded sample (Fig.1(b)), which showed the microstructural changes in different areas. The experimental details were summarised in the table, as shown in Fig. 1(c). The microstructure was characterised by scanning electron microscopy, using a Jeol-7100F equipped with an electron backscatter diffraction (EBSD) detector (a Thermo Fisher Lumis system) at the University of Surrey. An accelerating voltage of 20 kV and a beam current of 12 nA were used for EBSD, for which exposure time was ∼20 ms. Pixel binning of 2 × 2 and step size of 0.6 μm was used to collect the EBSD orientation maps (512 × 384 pixels). The denoising and filling non-indexing position processes were conducted by interpolating EBSD data using the MATLAB package MTEX 5.2.8 [33]. To account for the grain size, the grain boundary was reconstructed by smoothing the small grains with less than five pixels and the disorientation between grains with lower than 15° The micro-hardness characterisation was conducted using a nanoindenter (Agilent G200) with a Berkovich indenter tip at the UKAEA's Materials Research Facility. Strain rate-controlled indentations were carried out to 2 μm depth using continuous stiffness mode (2 nm amplitude, 45 Hz frequency, 0.05/s strain rate) and made in a 2 × 18 array across the welds in steps of 200 μm. The micro-hardness values reported were an average of the depth-resolved hardness from 1000 to 2000 nm deep. The error bars showed the standard deviation of two indentations at the same column of the array. Furthermore, micro-hardness of stress-free state was also conducted on the teeth of the comb-shaped stress-free samples (#2 and #4) using the same equipment and setup.
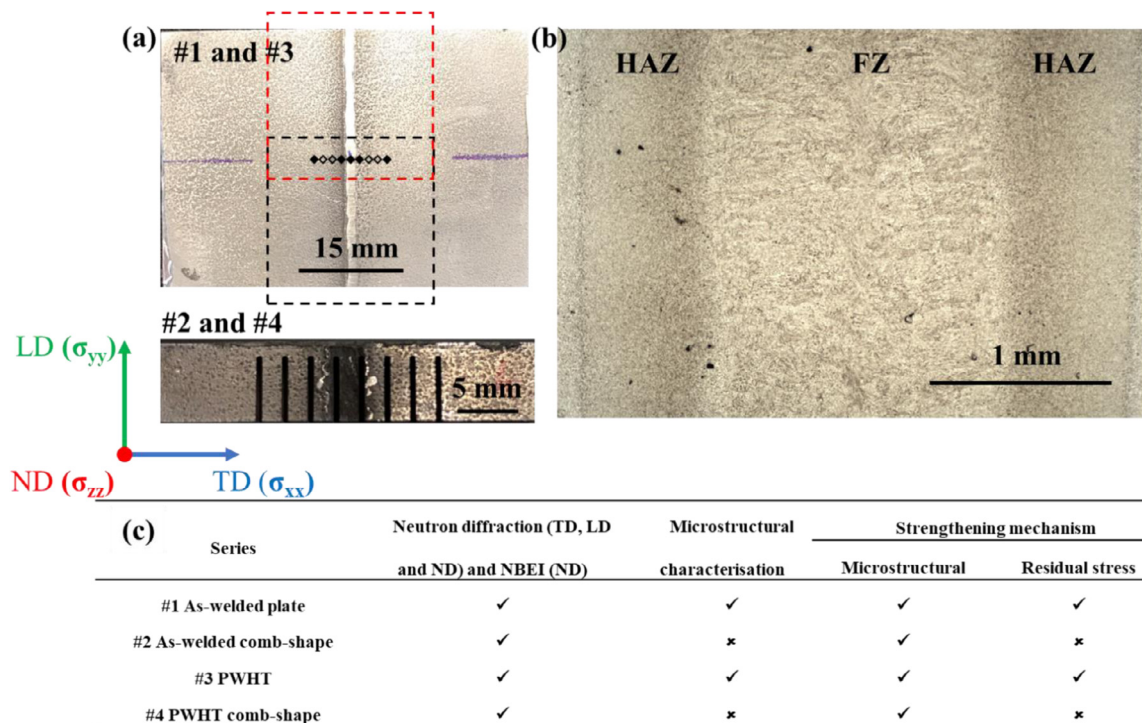
Fig. 1. (a) Optical micrographs of an as-welded sample (top left) and a comb-shaped sample (bottom left). The black diamond-shaped spots (top left) indicate the position where the neutron diffraction data were acquired, and the red and black dash rectangles (top left) show the position of the residual strain maps using NBEI. (b) Optical microscopy image of distinct FZ and HAZ regions of the top view of the as-welded sample. (c) Table for introducing the sample status and experimental arrangements.

2.2. Neutron diffraction

The residual lattice strain of both as-welded and PWHT samples along the longitudinal (LD), transverse (TD) and normal (ND) directions was measured by TOF neutron diffraction at the ENGIN-X beamline, Rutherford Appleton Laboratory, ISIS Neutron Source, UK. Fig. 1 shows the positions of the residual lattice strain measurements. There are nine data acquisition positions (unfilled and filled diamonds) for the as-welded sample, and five (filled diamonds) for the PWHT sample because the residual stress in the BM region is considered uniformly distributed after PWHT. Fig. 2(a) shows a schematic of the experimental setup, where two detectors collect the diffracted neutrons at ± 90° relative to the incident beam. Two procedures were used to measure the lattice spacing in three dimensions. The sample was firstly mounted horizontally and orientated at 45° relative to the incident neutron beam. As shown in Fig. 2(a), the through-thickness measurements are performed on the segment of the as-welded and the PWHT samples at distances of 1.72, 3.13 and 4.54 mm from the surface on which the beam was incident. The neutron beam dimension is $1 \times 1 \times 2$ mm³, defined by a 1×1 mm² incident slit and a 2 mm wide receiving radial collimator. This enables a resolution of 1.41 mm for residual stress measurementin the measured direction. To obtain sufficient neutron statistics for data analysis, neutron counts were acquired for 30 min at each data acquisition position in the HAZ and BM regions, and 45 min was chosen for collection at the data points in the FZ region. The axial detector recorded the strain along with TD, while the radial detector recorded the strain along with ND. In order to calculate the residual stress in three dimensions, the sample was rotated 90° around the ND axis to measure the strain along with the LD acquired by the axial bank and the acquisition time remained the same for each region. The residual stress measurements in three directions were performed on the same segment and position for both as-welded and PWHT samples by the same setup. The as-welded and PWHT comb-shaped stress-free samples,

in which the macroscopic residual stress was assumed to be fully relieved, were measured in three directions at the 1.72 mm from the top surface to determine the reference lattice spacing, d_0. Data were analysed by Rietveld refinement via routines written in Open Genie [34–36]. As shown in Fig. 2(b), the lattice spacing of each crystal plane is obtained using single-peak fitting (a Voigt peak shape combined with an exponential function) with consideration of elastic anisotropy [37,38]. To study the macro- residual stress and cross-validate the NBEI technique, the lattice spacing of {110} and {211} planes were selected for calculating the residual stress. The residual strain ε^{hkl} was determined by Eq. (1):

$$\varepsilon^{hkl} = \frac{d^{hkl} - d_0^{hkl}}{d_0^{hkl}} \tag{1}$$

where d^{hkl} is the lattice spacing and d_0 is the stress-free lattice spacing.

The stiffness tensor formed by elastic constants and presented in Voigt matrix notation shows the relationship between lattice strain and stress [39]. There are three independent fourth-order elastic constants for BCC structures and the values of the three for Eurofer97 are $C_{11} = 285.2$ GPa, $C_{12} = 125.9$ GPa and $C_{44} = 120.3$ GPa [4]. The stiffness tensors in the crystal reference frame ({110} and {211}) were derived from the stiffness tensor in the specimen reference frame by transforming the matrix according to Bunge angles [39]. The Bunge angles for {110}[110] and {211}[211] diffraction planes were calculated by using MATLAB, and the stiffness tensors in the crystal reference frame were calculated by Eq. (2):

$$[C_{hkl}] = [C][R_{hkl}] \tag{2}$$

where $[C]$ is the stiffness tensor in the specimen reference system, $[C_{hkl}]$ is the stiffness tensor in the crystal reference frame and $[R_{hlk}]$ is the transformation matrix according to Bunge angles of diffraction planes. The lattice stress for specific diffraction planes was
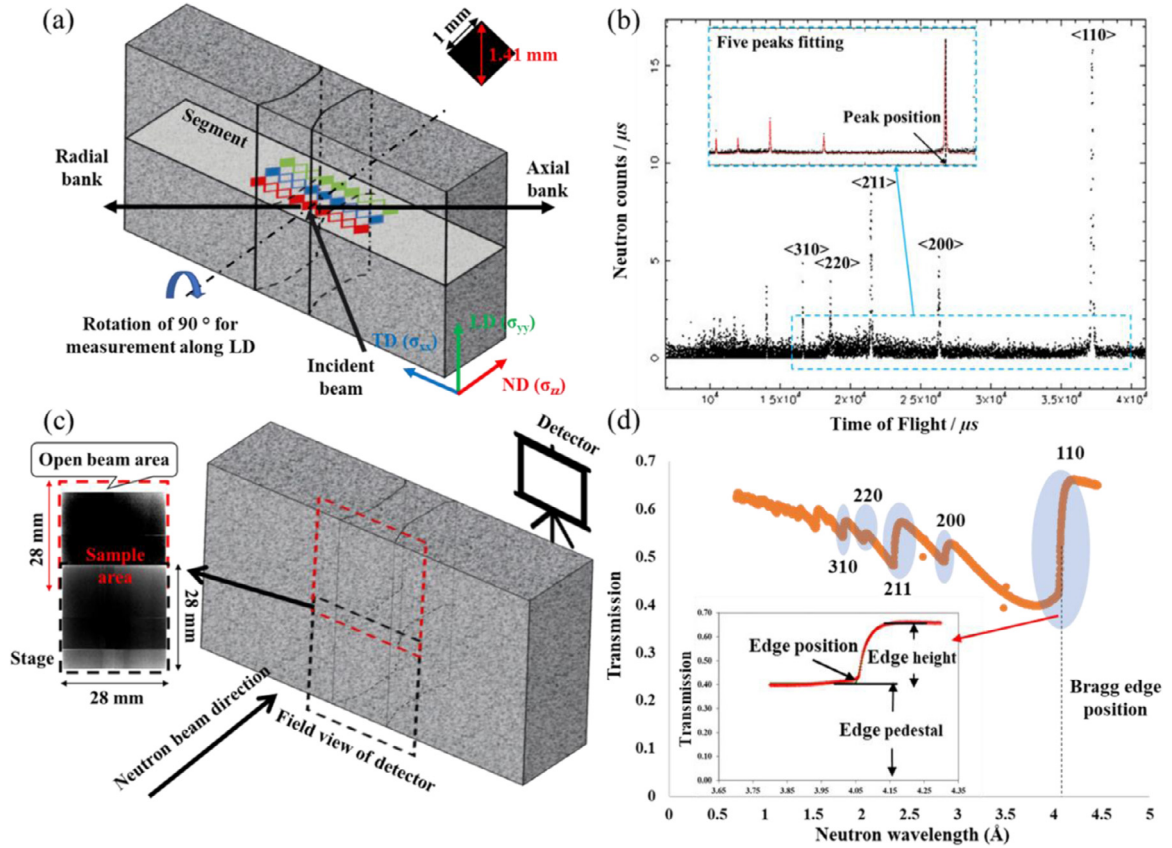
Fig. 2. (a) A schematic of the neutron diffraction experiment setup and data acquisition position. Three through-thickness line-scans at different distances to beam incident surface were performed. The data was acquired at both filled- and unfilled-spots position for the as-welded sample, while only at filled-spot positions for the PWHT sample. The diffraction data was recorded by two detector banks, labelled 'axial' and 'radial', yielding the strains along TD and ND. In order to measure residual stress along LD, the sample was rotated 90 ° around ND, and three line-scans were performed at the same data acquisition position. (b) Lattice spacings were extracted by peak fitting. (c) Neutron Bragg edge imaging (NBEI) experiment setup. The red and black dashed rectangles illustrate the two mapped areas that cover the welding affected region. The two images on the left are the transmission data recorded and saved by the detector. (d) An example of Bragg edge fitting for the {110} crystal plane. The Bragg edge position is obtained as one of five fitting parameters: edge position, edge height, edge width, edge pedestal and edge asymmetry (equipment parameter).

then determined by Hooke's law (Eq. (3)):

$$
\begin{bmatrix} \sigma_{hkl}^{TD} \\ \sigma_{hkl}^{LD} \\ \sigma_{hkl}^{ND} \end{bmatrix} = [C_{hkl}] \begin{bmatrix} \varepsilon_{hkl}^{TD} \\ \varepsilon_{hkl}^{LD} \\ \varepsilon_{hkl}^{ND} \end{bmatrix}
\tag{3}
$$

2.3. Neutron Bragg edge imaging (NBEI)

The NBEI experiment was conducted at the IMAT (Imaging and Materials instrument) beamline at Rutherford Appleton Laboratory, ISIS, UK [28]. An microchannel plate (MCP) detector with a field view of 28 × 28 mm^2 and pixel resolution of 55 μm (512 × 512 pixels) was used as the TOF imaging camera [27]. The strain map with a spatial resolution of ∼ 200 μm was measured by the TOF method with an L/D value of 166, where L is the distance from the pinhole collimator to sample and D is aperture diameter [40]. A ferritic steel standard was measured first to calibrate the length of the flight path [28,41]. Two maps were then collected on each sample, as-welded and PWHT, with ∼5 mm overlap, illustrated by red and black rectangles (see Fig. 2(c)). The reference lattice spacing was also measured by using comb-shaped stress-free samples. An open-beam data set was acquired, with the sample removed. A stack of 2881 radiographs were collected for each run, requiring four hours for adequate neutron counting statistics. The image stacks of the sample data and the open-beam data stacks were processed by using ImageJ [42], to obtain transmission maps by dividing the sample stack by the open beam stack. As shown in Fig. 2(d), a Bragg edge spectrum is then plotted as function of

wavelength, for a single pixel, combined 'macro-pixel' composed of several pixels, or a larger region of interest. The position of a Bragg edge was determined by fitting the Bragg edge spectrum via an analytical function [43,44] (Eq. (4)):

$$
T(\lambda) = C_1 + C_2 \left[\mathrm{erfc}\left(\frac{\lambda_0 - \lambda}{\sqrt{2}\sigma} \right) - \exp\left(\frac{\lambda_0 - \lambda}{\tau} + \frac{\sigma^2}{2\tau^2} \right) \right.
$$
$$
\left. \times \mathbf{erfc}\left(\frac{\lambda_0 - \lambda}{\sqrt{2}\sigma} + \frac{\sigma}{\sqrt{2}\tau} \right) \right]
\tag{4}
$$

where λ is lambda edge position, σ is the Bragg edge width, τ is the edge asymmetry, C_1 is edge height and C_2 is edge pedestal (see inset Fig 2(d)). The residual strain was determined pixel-by-pixel according to the Bragg edge position by using Eq. (5), and the map was generated by a C++ fitting tool, TPX_edgefit, by using a macro-pixel size of 5 pixels and a running average with steps of 55 um [41]. The reference Bragg edge position was extracted from the teeth of comb-shaped samples at the FZ, HAZ and BM regions.

$$
\varepsilon^{hkl} = \frac{\lambda^{hkl} - \lambda_0^{hkl}}{\lambda_0^{hkl}}
\tag{5}
$$

where λ is the Bragg edge position of the sample, λ_0 is the reference Bragg edge position. It is worth noting that the NBEI yields the strain component in the beam direction only (i.e. ND).
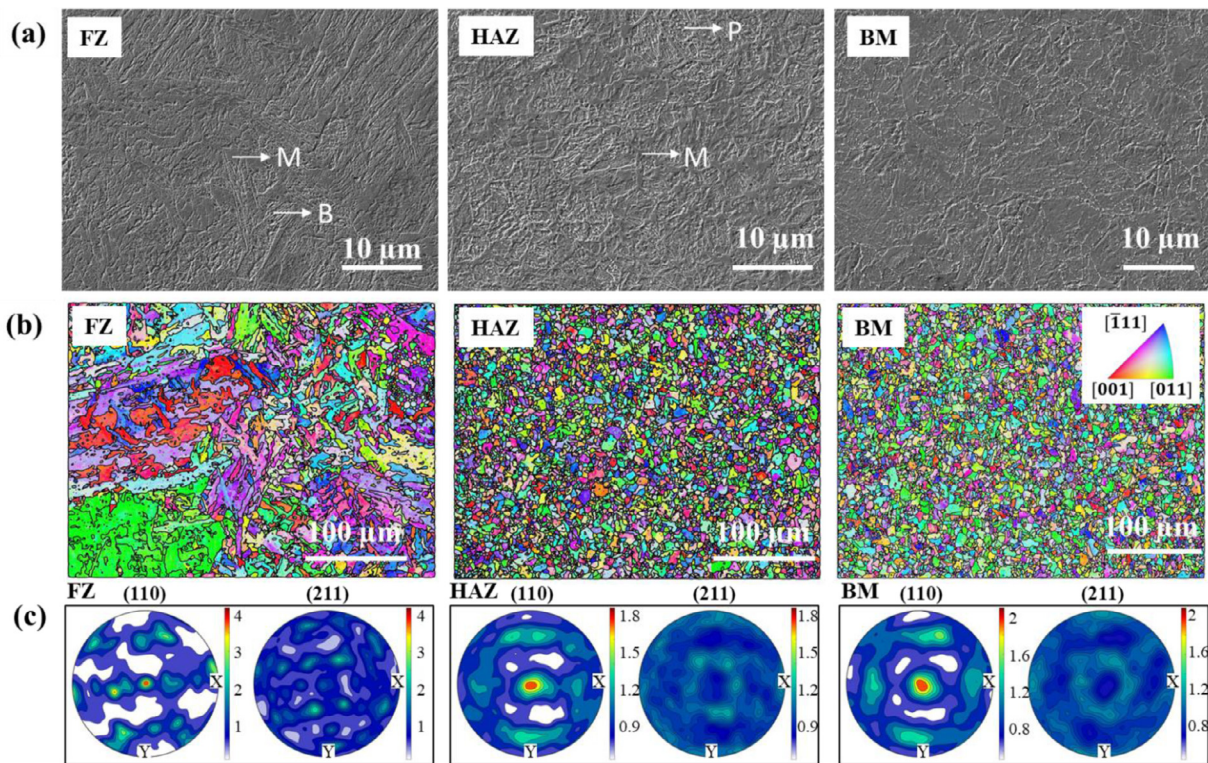
Fig. 3. Microstructure of as-welded sample. (a) Microstructure at FZ, HAZ and BM regions acquired by SEM. The lath-like bainite, martensite and precipitate are labelled by B, M and P, respectively. (b) EBSD maps at the FZ, HAZ and BM regions. (c) Corresponding PF at the FZ, HAZ and BM regions, where the X direction is the TD, the Y direction the LD and the map normals are the ND.
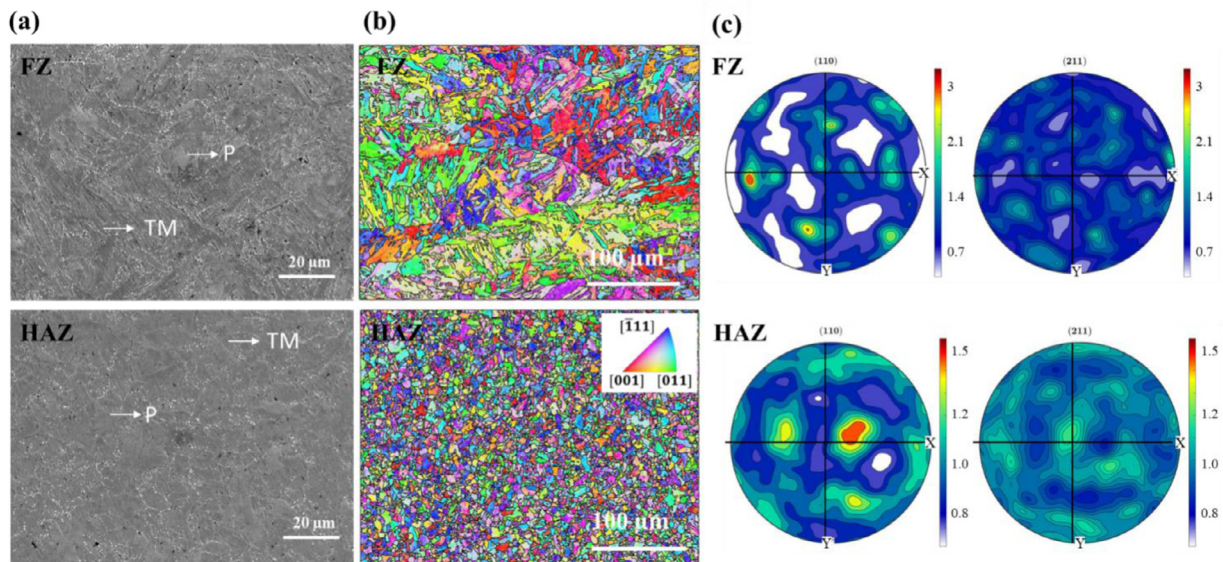

Fig. 4. Microstructure of the PWHT sample. (a) Microstructure at FZ and HAZ regions after PWHT acquired by the SEM. The tempered martensite and precipitate are labelled as TM and P, respectively. (b) EBSD maps of PWHT sample at FZ and HAZ regions. (c) PF derived from relative EBSD maps at FZ and HAZ regions where the coordinate of X is TD, Y is LD, and the centre is ND.

3. Results

3.1. Microstructural characterisation

Figs. 3 and 4 show the microstructure across the welds of as-welded and PWHT samples, respectively. In Fig. 3(a) and (b), the SEM images and EBSD maps show that the martensite laths and lath-like bainite within the irregularly columnar prior-austenite grains (PAGs) are formed in the FZ region, whereas equiaxed PAGs

with martensite laths and precipitates (carbides) are presented in the HAZ and BM regions. Because of partial austenitisation and tempering in the HAZ region, the quenched and tempered martensite are observed together. In the BM region, PAG boundaries and tempered martensite are decorated by a large number of carbides, essentially an identical microstructure to the as-received Eurofer97 [45]. The PAG sizes of the FZ, HAZ and BM regions are determined by the EBSD maps in Fig. 3(b) by using the mean linear intercept method [46]. The PAG size is found to significantly decrease from

15.2 $\pm$ 2.8 μm in the FZ region to 5.9 $\pm$ 0.8 μm in the HAZ region, then increase in the BM region to 7.3 $\pm$ 0.9 μm. Fig. 3(c) displays the pole figures (PF) of the (110) and (211) crystal plane normal of the FZ and HAZ regions. It is evident that the (110) crystal plane exhibits a stronger texture in the FZ region, which reaches around 4 multiples of a random distribution (MRD), but the intensity in the HAZ region decreases to around 1.8 MRD. Additionally, the highest intensities of (110) plane normals in both FZ and HAZ regions occur along the direction parallel to the ND in the specimen reference frame. In contrast, the highest pole densities of (211) in both FZ and HAZ regions are lower than those of the (110) crystal plane, which are around 2.2 and 1.2 MRD, respectively.

Compared to the as-welded sample, fine precipitates are observed in the FZ region after PWHT (Fig. 4(a)). Fig. 4(b) shows the grain orientation and sizes of the PWHT sample in the FZ and HAZ regions, where the PAG size almost remains the same after PWHT. The PFs in Fig. 4(c) show that the {110} planes are still textured in the FZ region, with pole density maxima ~3 MRD, while moving to the HAZ region, the intensity of texture decreases to the 1.5 MRD. By contrast, the texture of {211} plane is significantly lower in the FZ and HAZ regions, where the highest intensities are ~ 2 and ~ 1.2 MRD, respectively. As such, the pole density distribution is similar to that of the as-welded sample.

3.2. Residual stress distribution revealed by neutron diffraction

The lattice spacings corresponding to crystal planes {211} was used to calculate the residual stress, as such crystal plane was recommended to represent the residual stress on the macro-scale for body centred cubic structures [47,48]. The {110} crystal plane that had the highest intenstity over the peaks was also analysed to cross-validate the results from the neutron diffraction and NBEI. The through-thickness residual stress profiles in three dimensions of the as-welded and PWHT samples are shown in Fig. 5(a) and Fig. 6(a), respectively. The uncertainty in the measured residual strains are approximately $\pm$ 30 $\mu\varepsilon$ [49,50]. The σ_{xx}, σ_{yy} and σ_{zz} represent the residual stress along TD, LD and ND, respectively, and the red, blue and green symbols and lines represent the residual stress at different distances from the beam incident surface. The residual stress profiles in Fig. 5(a$_1$) and Fig. 5(a$_2$) show similar 'M-shaped' symmetry. The highest residual stress derived from {211} crystal plane is σ_{yy}, 580 MPa, whereas the smaller residual stress is found to be both σ_{xx} and σ_{zz} residual stress components, which are in a similar magnitude. Additionally, the residual stress in the FZ region derived from {211} planes is larger than that from {110} diffraction planes.

Residual stress maps of σ_{xx}, σ_{yy} and σ_{zz} components on the segment plane of the as-welded and PWHT sample are plotted with the values from neutron diffraction measurements by using interpolation method by MATLAB in Fig. 5(b) and Fig. 6(b), respectively, using the three through-thickness line-scan measurements. As illustrated in Fig. 5(b), the residual stress follows a similar distribution at different distances from the beam incident surface, and the σ_{yy} is obviously higher than in other directions, and compressive residual stress is found within the FZ region. Moving away from the centre, the residual stress gradually changes, reaching tension and eventually decreasing to zero in the BM region.

Fig. 6(a) indicates that the residual stress has been relaxed significantly after PWHT. Although the values are very low, the residual stress still exists around the welding centre, ranging from -50 MPa to 100 MPa. In general, the profiles of the residual stress in three dimensions are of a similar magnitude and follow the same overall trend. For the {211} planes (Fig. 6(a$_1$)), the blue residual lattice stress profile is different in shape, compared with the red and the green curves, while they are similar for the {110} planes (Fig. 6(a$_2$)). Fig. 6(b) shows the residual stress maps of the mea-

sured segment plane, which illustrates that the residual stress has been significantly relieved.

3.3. Residual strain distribution revealed by neutron Bragg edge imaging (NBEI)

The HR-NBEI residual strain maps derived from {211} and {110} diffraction planes along ND of the as-welded sample are shown in Fig. 7(a$_1$) and (a$_3$), respectively. The spatial resolution of the HR-NBEI map is about 200 μm due to the large macro-pixel size used in combination with a running average. Both figures show that the distinct compressive residual lattice strain distributes around the centre line of the weld and is balanced by tensile lattice strain further away. Looked along the welding direction, the residual strain distribution is of the same sign but less variable.

To enable the comparison and cross-validation between the neutron diffraction and NBEI, the HR- NBEI residual strain maps were converted to the low resolution (LR-) residual strain maps Fig. 7(a$_2$) and (a$_4$) with the spatial resolution of 1.4 mm by averaging the residual strain over the surrounding pixels in the map, which is same as the gauge volume of neutron diffraction. Similarly, the residual strains measured by neutron diffraction were averaged through the sample thickness. Both HR- and LR- NBEI residual strain maps in the region (cuboid in Fig. 7(a)) measured by both techniques are converted to profiles with the same spatial resolution as the maps and plotted in Fig. 7(b). Compared to the LR-NBEI profile, the HR-NBEI shows the detailed distribution at the interface between FZ, HAZ and BM regions. The results of LR-NBEI are consistent with that of neutron diffraction, while the magnitude of compressive residual strain in the FZ region is slightly lower. The residual strain maps and profiles for the {211} and {110} planes of the PWHT sample are plotted in Fig. 8 in the same manner. The residual strain reduces significantly after the PWHT. However, approximately 300 $\mu\varepsilon$ strain still appears in the FZ region at both {110} and {211} planes, as shown in Fig. 8(b$_1$) and (b$_2$).

Fig. 7(c) shows a comparison of the Bragg edge between FZ and BM regions. Compared to the Bragg edge in the BM region, the Bragg edge in the FZ region shows the edge broadening for both {110} and {211} planes due to the micro-strain, while the edge shape changes are observed for the {110} plane due to the preferred crystallographic orientation [29]. Fig. 8(c) shows the microstructure in the FZ region is very similar to that of the BM regions for the {211} plane, whereas the slight difference is found at the edge broadening and edge shape for the {110} plane.

3.4. Micro-hardness characterisation

The micro-hardness values of the as-welded, PWHT and comb-shaped stress-free samples across the weldments were measured, and these data are summarised in Fig. 9(a). The micro-hardness profile of the as-welded sample increases from 2.75 $\pm$ 0.09 GPa in the BM region to 5.06 $\pm$ 0.29 GPa in FZ and HAZ regions, respectively. The hardness values in the FZ and HAZ regions reduce significantly after the PWHT to 3.25 $\pm$ 0.11 GPa. A gradual drop is found in the HAZ region on both as-welded and PWHT samples. The lowest micro-hardness interface occurs at the interface between the HAZ and BM on the PWHT sample. The micro-hardness at stress-free state is obtained by performing the nanoindentation at the teeth of comb-shaped stress-free samples (Fig. 9(a)), which illustrates a similar hardness value in the FZ and BM regions. This indicates that the micro-hardness values are dominated by micro-residual stresses which are still preserved in the comb-shaped stress-free samples. The effect of residual stress and microstructure on micro-hardness is evident in Fig. 9(b) and (c), which illustrates the micro-hardness differences in the HAZ and FZ regions by comparing the load-displacement curves of as-welded and PWHT sam-
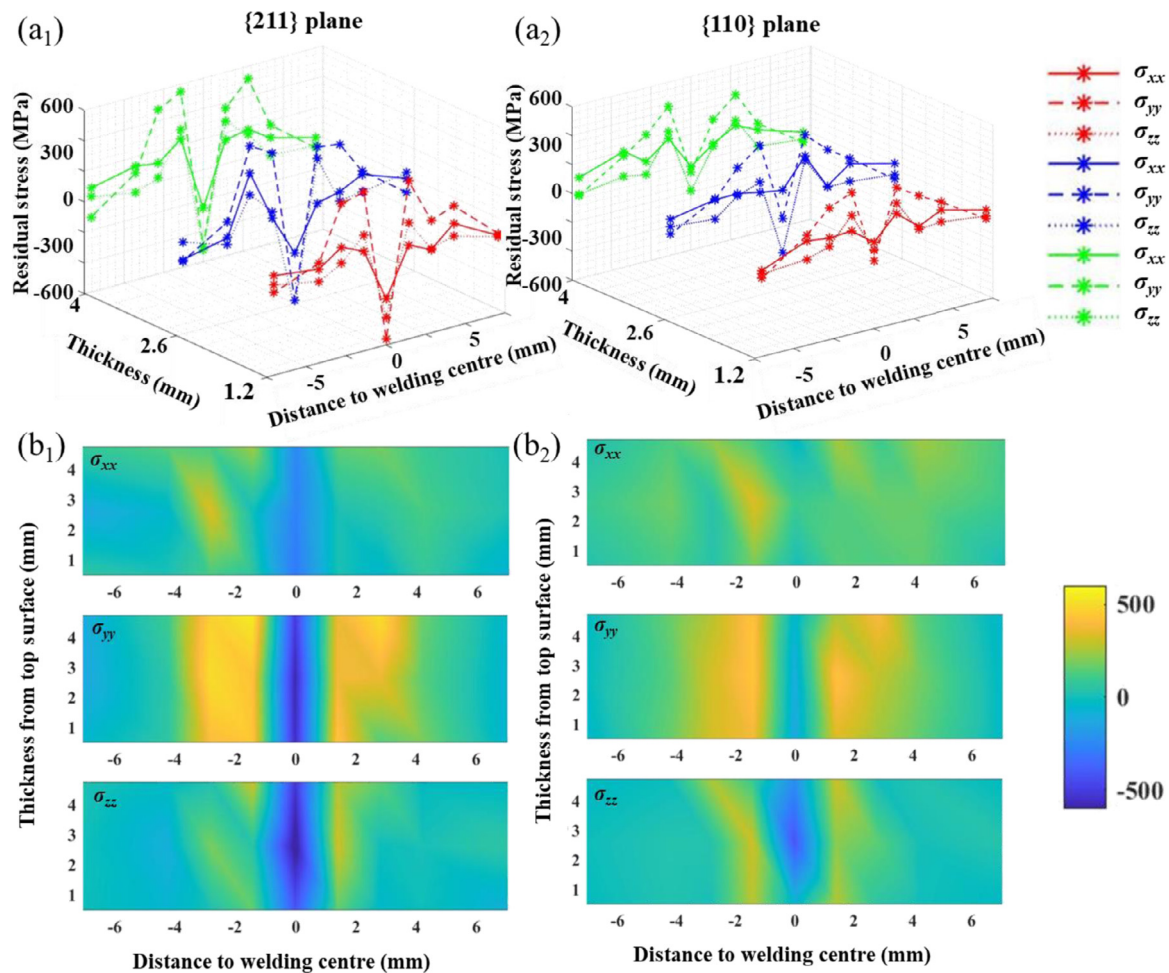
Fig. 5. Residual stress of σ_{xx}, σ_{yy} and σ_{zz} components of as-welded sample derived from neutron diffraction by a single-peak fitting approach. (a) The through-thickness residual stress distribution extracted at three different distances to beam incident surface. (b) The residual stress on the segment plane.

ples. This difference is attributed to both the microstructure and residual stress hardening. A comparison with the curve for the BM enables the total hardening and hardening caused by PWHT microstructure to be obtained. Fig. 9(d) illustrates that the full width half maximum (FWHM) distributions of both as-welded and PWHT samples are extracted at the thickness of 1.72 mm to the top surface in three directions. The trend of the peak broadening is similar in three directions, where significant broadening is observed around the welding region, indicating the microstructural changes during welding processes.

4. Discussion

4.1. Residual lattice stress and strain distributions across FZ, HAZ and BM regions

All the profiles in Figs. 5(a) and 7(a) show that the residual stress caused by the single laser welding acts over approximately 4 mm from the welding centre, and manifests itself in an M-shaped distribution; strongly in compression in the FZ region (∼ -600 MPa) and changing to tension and reaching maximum in the BM region (∼ +600 MPa) just outside the HAZ. The shrinkage, quench-induced martensitic phase transformation and the γ-α phase transformation during the cooling affect both the magnitude and shape of the residual stress profile [51,52]. As a result of high heat input and the rapid cooling process of laser welding,

the shrinkage and phase transformation effectively occur simultaneously contributing to the M-shaped residual stress profile.

The residual stress distribution in Fig. 5(a) also illustrates a similar magnitude and trend at different thicknesses. This indicates full penetration of the sample during welding generates similar widths of FZ and HAZ regions. Similar results are also found in ferritic steel welded by high heat-input joining techniques [22]. Comparison of the residual lattice stresses in the three directions, TD, LD and ND, (Fig. 5(b)), reveals that the transverse and normal residual stress profiles are similarly M-shaped like the longitudinal profile, but exhibit lower tensile residual stress levels as expected. This is attributed to the unbalanced compressive plastic flow that occurs in front of the weld pool during the welding thermal cycle leading to a higher tensile residual stress at the interface of the HAZ and BM which is in agreement with data obtained from laser-welded P91 steel [13].

Although the residual stress profiles derived from {211} and {110} crystal planes exhibit the same trend, the magnitudes differ to a small extent (Fig. 5(a)). Micro-residual stress in the materials can result, for example, from the plastic deformation of a material, leading to both peak shift and peak broadening [47]. Different crystal planes have different sensitivities to micro-stress. The {211} crystal plane is usually recommended to represent the residual stress on the macro-scale for body centre cubic structures [47]. On the other hand, similar difference of two crystal planes is also observed in the both HR- and LR- NBEI strain profiles (Figs. 7(b) and 8(b)) where the magnitude of {211} is higher than that of
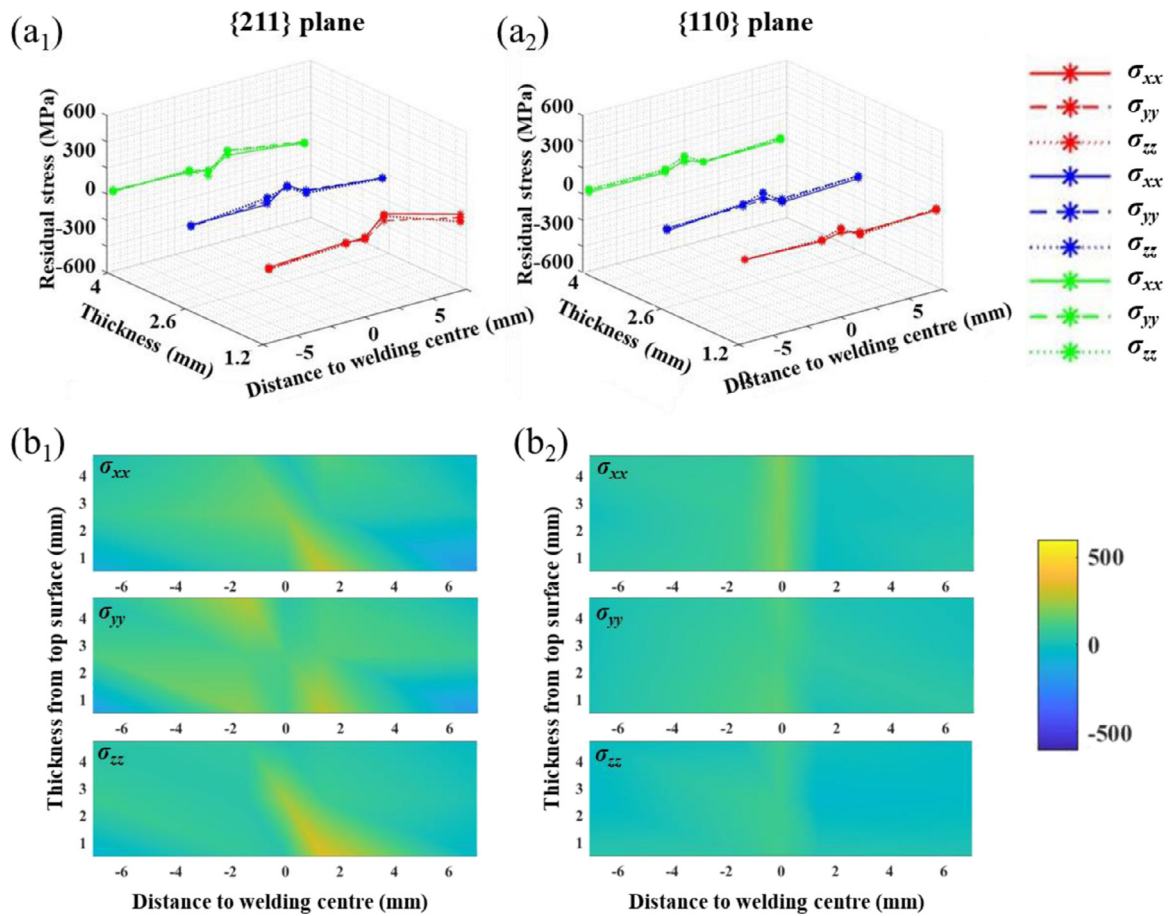
Fig. 6. Residual stress of σ_{xx}, σ_{yy} and σ_{zz} components of the PWHT sample derived from neutron diffraction by single-peak analyses. (a) The through-thickness residual stress distribution extracted at three different distances to beam incident surface. (b) The residual stress on the segment plane.
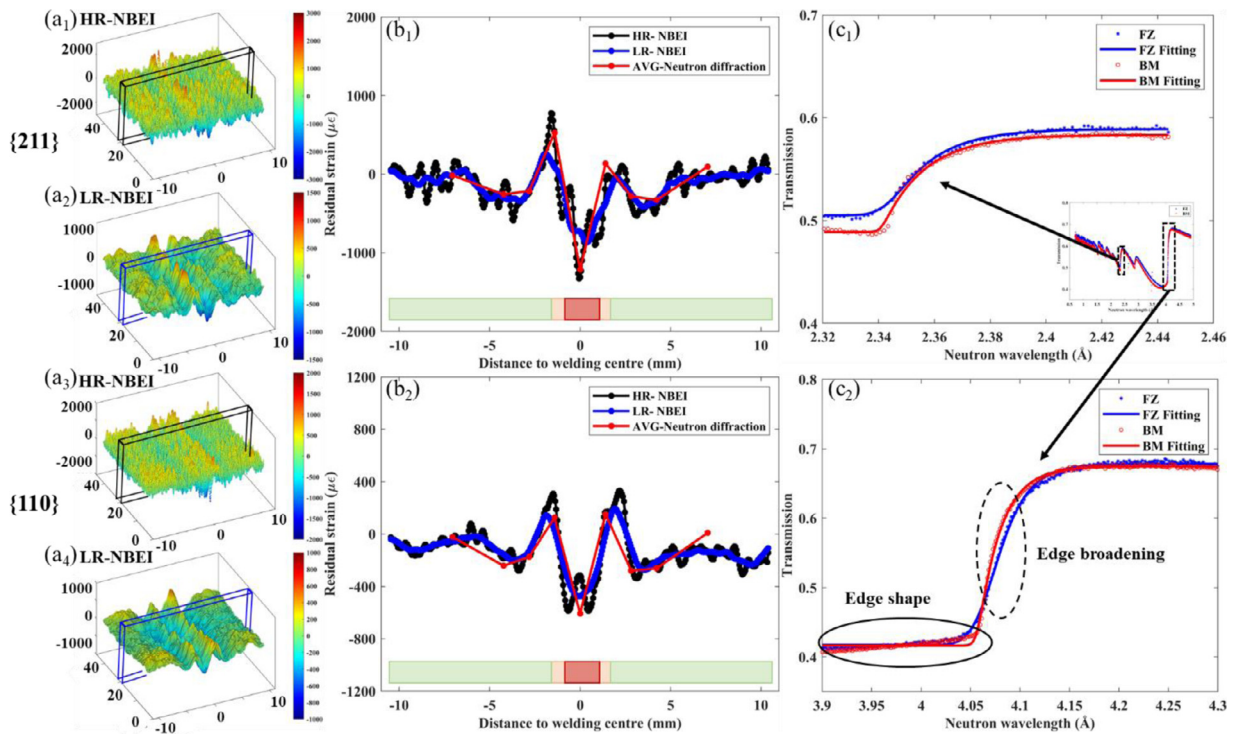

Fig. 7. Residual strain maps and profiles of the as-welded sample measured by NBEI. (a_1), (a_2), (a_3)and (a_4) Strain maps along ND calculated from lattice spacings of {211} and {110} planes. (b_1) and (b_2) Comparison of residual strain distribution of {211} and {110} crystal planes which are measured by NBEI and neutron diffraction, respectively. (c_1) and (c_2) Comparison of Bragg edges of {211} and {110} crystal planes in the FZ and BM regions, respectively.
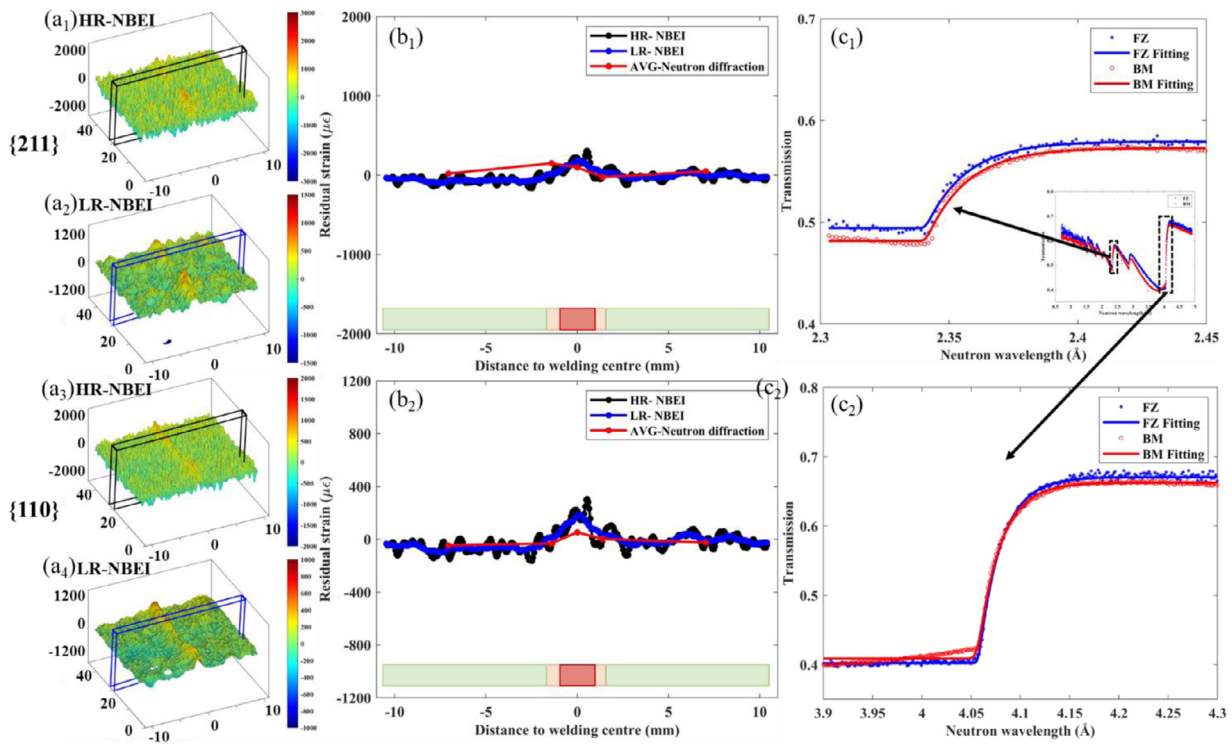
Fig. 8. Residual strain maps and strain profiles of the PWHT sample measured by NBEI.(a_1), (a_2), (a_3)and (a_4) Strain maps along ND (b_1) and (b_2) Comparison of residual strain distribution of {211} and {110} crystal planes which are measured by NBEI and neutron diffraction, respectively. (c_1) and (c_2) Comparison of Bragg edges of {211} and {110} crystal planes in the FZ and BM regions, respectively. The residual strain are plotted in the same way as in Fig. 7.
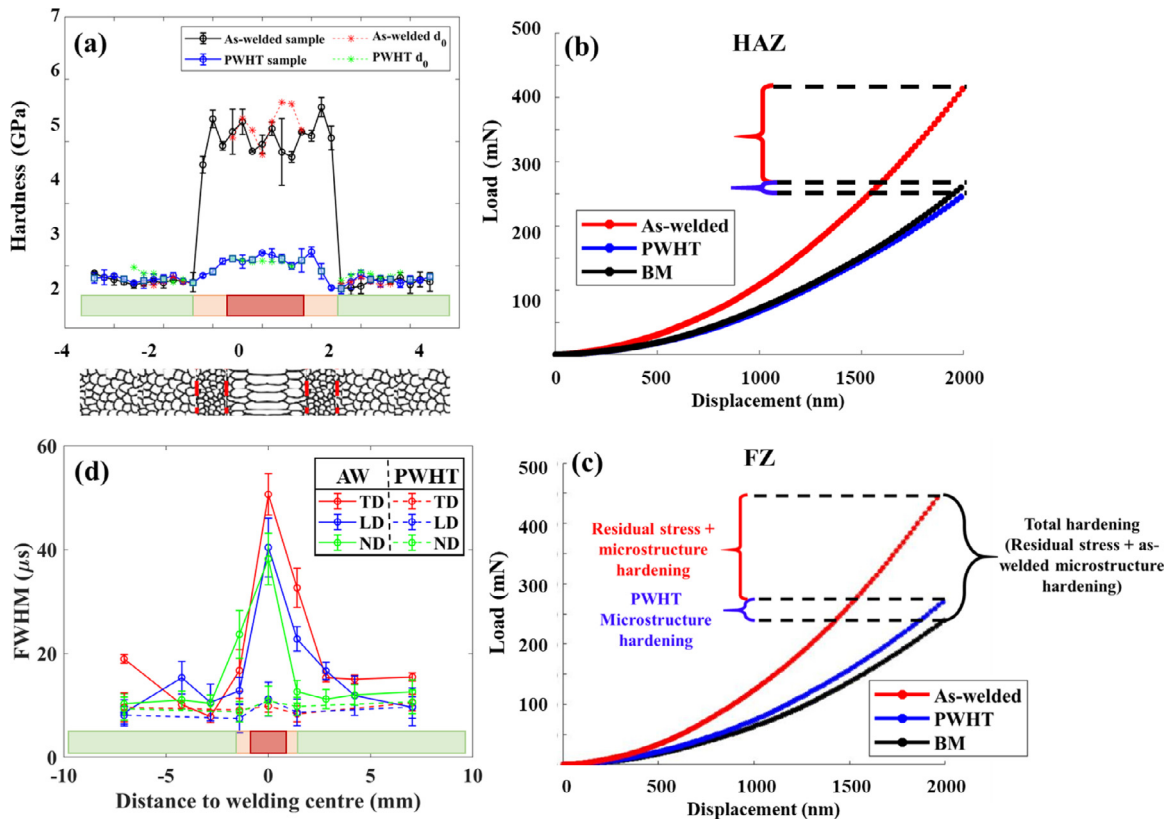

Fig. 9. (a) Micro-hardness distribution in the as-welded and PWHT samples correlated with the crystal size in the FZ, HAZ and BM. The micro-hardness at the teeth of comb-shaped reference sample is also included, which is labelled as as-welded d_0 and PWHT d_0. (b) and (c) Load-displacement curves derived from the FZ, HAZ and BM of the as-welded and PWHT samples, respectively. (d) The FWHM distribtution across the welding region of both as-welded and PWHT samples extracted at the thickness of 1.72 mm from the top surface.

{110} crystal plane. Compared to the Bragg edges in the BM region (Fig. 7(c)), the edge broadening is observed for both {211} and {110} crystal planes in the welding region, which also suggests the existence of the micro-stress.

PWHT is usually applied to modify the as-welded microstructure and relax residual welding stresses to impart reproducible properties and predictable integrity, although the fabrication technologies for the EU DEMO in-vessel components have not been finalised [53]. The neutron diffraction measurements demonstrate that the high residual stress is largely relieved in the PWHT sample, showing that PWHT is effective in relaxing residual stresses, as shown in Figs. 6 and 8. The small extent of tensile residual strain appears in the FZ region. The Cr-enriched $M_{23}C_6$ carbide and V-enriched MX carbide can be formed in the FZ region after PWHT at 750 °C, which is primarily the reason to induce local micro-strain [54,55]. Fig. 4(e) and (f) shows slightly lower pole densities in the PWHT sample than those in the as-welded sample. Similar results are derived from comparison of Bragg edge shape (Fig. 8(c)) in FZ and BM regions. Although the microstructures, e.g., grain size and texture, are not fully restored, the selective PWHT substantially relaxes the residual stress.

The current single-pass laser welding induces narrower FZ and HAZ (~5 mm) than a hybrid laser-welded Eurofer97 steel (~12 mm), with a power of 4 kW [12]. However, the magnitude of the residual stresses is similar in both welded samples. A similar phenomenon is also found in the single laser and hybrid laser-welded P91 steel with 7 kW heat input, where narrower FZ and HAZ are generated by single-pass laser welding but the residual stresses induced by the two techniques are similar [56].

4.2. Comparison between neutron diffraction and neutron Bragg edge imaging

Both techniques measure the strain by using a TOF method, providing information from the interior but with different spatial resolution and gauge volume. Neutron diffraction measures the through-thickness strain in three orthogonal directions by using a gauge volume length of 1.41 mm by controlling the incident slits and by using a radial collimator (see inset Fig. 2(a)), whereas for NBEI the strain is averaged over the whole chord through the sample along the beam direction (ND). The spatial resolution of ~200 μm for NBEI is controlled by the value of *L/D* and the choice of the macro-pixel binning of the 55 μm pixels of the MCP detector. Due to the high spatial resolution achieved, the NBEI residual strain measurement is more sensitive to the changes of texture and grain size than the neutron diffraction [57]. As shown in HR-NBEI profiles in Figs. 7(b) and 8(b), the residual strain distributions vary at the narrow interface of FZ-HAZ and HAZ-BM regions, resulting from the sharp changes of grain size. The LR-NBEI profile is in good agreement with the AVG-neutron diffraction profile of both as-welded and PWHT samples (red line in Fig. 7(b) and 8(b)).

Minor differences in magnitude are observed between the two techniques in the FZ region. This discrepancy is attributed to the existence of local differences in texture because the texture can change the Bragg edge shape [57]. The BM region in the as-welded sample is assumed as texture-free region. Compared to the Bragg edge of BM (Fig. 7(c)), the edge shape changes in both crystal planes indicate the texture evolution in the FZ and HAZ. The more distinct edge shape changes of {110} planes indicate the intense texture, which is also consistent with the results from the EBSD. This change affects the fitting of Bragg edge position, which should have been defined exclusively by the planes orientated perpendicular to the incident beam [58,59]. The peak fitting for neutron diffraction is, however, less affected in the FZ region, which does highlight that Bragg edge fitting for NBEI is much more sensitive to texture than Bragg peak fitting for neutron diffraction. After the

PWHT, according to the Bragg edge shape, the FZ region becomes texture-free for {211} crystal plane, the residual lattice strain is consistent with the neutron diffraction, as shown in Fig. 8(b_1). Although it seems that the neutron diffraction has fewer uncertainties than the NBEI technique in residual strain measurement, the NBEI technique is entitled to unique strength in mapping residual strain, which is indispensable for analysing the mechanical degrades of the materials in large areas. It is expected that the combination of the advantages of neutron diffraction and NBEI can be a powerful tool for non-destructive residual stress analysis.

Residual stress/strain distributions obtained from neutron diffraction and NBEI measurements in the current study are contrary to those from previous studies which have suggested that the residual stress of hybrid-laser welded Eurofer97 sample measured by neutron diffraction is tensile in the FZ region [12,24,60]. This difference most probably arises because the reference lattice spacing used in previous residual stress characterisation is from the far-field region of the weldment. Additionally, the sample dimension and parameters of the laser welding are different, leading to the difference in the heat input, penetration, width of the HAZ area and the weld pool geometry, which also affects the residual stress distribution.

There are four ways widely recommended for obtaining reference lattice spacings. These are measurement at a far-field welding unaffected region, measurement on a stress-free powder or filings, measurement on a thin cube, or use of the teeth of a comb with the application of stress balance [61]. As a result of the difference in thermal history during the welding, the inelastic strain and chemical composition vary with the position. Given that diffraction-based residual strain/stress measurements account for not only elastic strain but also inelastic strain, the using of a reference lattice spacing from far-field induces uncertainty in the FZ and HAZ regions [62,63]. Here, the lattice spacing from the teeth of the comb-shaped sample is employed to provide the location-dependant d_0 for both neutron diffraction and NBEI measurements, which corrects the effect of inelastic strain, chemical composition and microstructure in the residual strain calculation. A limitation of using the comb-shaped stress-free sample is that the residuals of micro-stress and limited resolution for the narrow HAZ in this research is due to the gap between the teeth.

4.3. Correlation of microstructure, micro-hardness and residual stress

Micro-hardness is sensitive to the microstructural changes taking place throughout the welds. Fig. 9 shows that the micro-hardness distributions of both as-welded and PWHT samples, from which the FZ and HAZ regions are significantly higher than that at BM region.(not clear in structure and meaning) This is attributed to the quenched martensite and lath-like bainite which is confined to the FZ, whereas the quenched martensite and precipitates dominate the HAZ (Fig. 3(a)). The micro-hardness increases slightly at the FZ-HAZ interface, as the PAG size in the FZ is larger than that in the HAZ by approximately three-fold, which in principle means a lower hardness according to Hall-Petch effect [64,65]. Moving to the BM region, since temperature excursion here is lower than the lower critical temperature (A_{c1}) and the tensile residual stress reaches a maximum, a steep drop in micro-hardness occurs. A similar phenomenon also occurrs with laser welded P91 steel [13]. The micro-hardness at the weld reduces significantly by the PWHT and the lowest micro-hardness is observed around the interface of HAZ-BM region. The reduction is attributed to the high temperature and low cooling rate during PWHT, which results in the formation of tempered martensite and coarsening of precipitates [66]. The PWHT causes a drop in dislocation density, which is evident in the decrease in FWHM in the welding region (Fig. 9(d)). In addition, the slightly higher micro-hardness in the FZ region is consis-

tent with the presence of lath-shaped martensitic features and the higher density of precipitates. A similar phenomenon is reported for welded Grade 91 steel where the same PWHT thermal cycle was applied [67].

Both microstructural variation and spatial variation in residual stress can affect the micro-hardness [68,69]. The micro-hardness reduces gradually from the HAZ region to the BM region due to partial/incomplete transformation of the tempered martensite and the increases of tensile residual stress in corresponding areas during the welding process. A comparison of load-displacement curves (Fig. 9(b)) in the BM region reveals the contributions of the residual stress and microstructure to the hardening phenomenon in the FZ region. However, only a small difference is found between as-welded and stress-free samples in the FZ region. This is attributed to high dislocation density induced by the martensitic transformation during the welding processes [70]. As shown in Fig. 9(d), the peak broadening around the welding centre implies the high dislocation density. Although the macro-scale residual stress in the comb-shaped sample has been released, the dislocation density remains the same. The nanoindentation measures the hardness value on a small scale where the microstructure's contribution dominates. A full model that can account for the effect of macro-scale residual stress relaxation on other mechanical properties, e.g. tensile strength, is necessary and will be the subject of future research.

5. Conclusions

The through-thickness residual stress and HR-strain field of as-welded and PWHT Eurofer97 samples were studied by using two neutron-based techniques. The as-welded sample shows an M-shaped residual stress profile and its magnitude in the longitudinal direction is the most significant: 595 MPa of compressive stress at the centre line of the FZ region and 580 MPa of tensile stress at the interface of HAZ and BM regions. Additionally, the strain maps show distinct differences in the FZ, HAZ and BM regions. The HR-residual strain profiles extracted from a map is in good agreement with the neutron diffraction data. Whilst there are principal limitations because of texture in these materials, better results can be achieved in future with neutron sources of higher brilliance, by improvements in transmission detector technology, and further development of Bragg edge data analysis tools. Furthermore, the understanding of the mechanistic connections between micro-hardness, microstructure and residual stress has been broadly established. The as-welded sample in the FZ region is hardened by microstructural features dominantly. Selective PWHT is capable of relieving the residual stress, but the microstructures are not fully restored. The material in the FZ and HAZ regions is still hardened by the lath-shaped martensitic phase and fine precipitates after PWHT.

Declaration of Competing Interest

The authors declare that they have no known competing financial interests or personal relationships that could have appeared to influence the work reported in this paper.

CRediT authorship contribution statement

Bin Zhu: Data curation, Formal analysis, Funding acquisition, Writing – original draft, Investigation. **Winfried Kockelmann:** Methodology. **Saurabh Kabra:** Methodology. **Andrew J. London:** Methodology. **Michael Gorley:** Conceptualization. **Mark J. Whiting:** Conceptualization, Writing – review & editing. **Yiqiang Wang:** Conceptualization, Writing – review & editing, Data curation, Funding acquisition. **Tan Sui:** Conceptualization, Writing – review & editing, Funding acquisition.

References

[1] P. Fernández, A.. Lancha, J. Lapeña, M. Serrano, M. Hernández-Mayoral, J. Nucl. Mater. 307–311 (2002) 495–499.

[2] A. Zeman, L. Debarberis, J. Kočík, V. Slugeň, E. Keilová, J. Nucl. Mater. 362 (2007) 259–267.

[3] S. Wu, J. Zhang, J. Yang, J. Lu, H. Liao, X. Wang, J. Nucl. Mater. 503 (2018) 66–74.

[4] X.X. Li, X.X. Li, S. Schönecker, R. Li, J. Zhao, L. Vitos, Understanding the Mechanical Properties of Reduced Activation Steels, Elsevier Ltd, 2018.

[5] R. Andreani, E. Diegele, R. Laesser, B. Van Der Schaaf, J. Nucl. Mater. 329-333 (2004) 20–30.

[6] R. Lässer, N. Baluc, J.L. Boutard, E. Diegele, S. Dudarev, M. Gasparotto, A. Möslang, R. Pippan, B. Riccardi, B. van der Schaaf, Fusion Eng. Des. 82 (2007) 511–520.

[7] M. Richardson, M. Gorley, Y. Wang, G. Aiello, G. Pintsuk, E. Gaganidze, M. Richou, J. Henry, R. Vila, M. Rieth, J. Nucl. Mater. 550 (2021) 152906.

[8] P. Aubert, F. Tavassoli, M. Rieth, E. Diegele, Y. Poitevin, J. Nucl. Mater. 409 (2011) 156–162.

[9] S. Kirk, W. Suder, K. Keogh, T. Tremethick, A. Loving, Fusion Eng. Des. 136 (2018) 612–616.

[10] H. Tanigawa, T. Maruyama, Y. Noguchi, N. Takeda, S. Kakudate, Fusion Eng. Des. 98–99 (2015) 1634–1637.

[11] P. Aubert, F. Tavassoli, M. Rieth, E. Diegele, Y. Poitevin, J. Nucl. Mater. 417 (2011) 43–50.

[12] D.J. Hughes, E. Koukovini-Platia, E.L. Heeley, Fusion Eng. Des. 89 (2014) 104–108.

[13] S. Kumar, A. Kundu, K.A. Venkata, A. Evans, C.E. Truman, J.A. Francis, K. Bhanumurthy, P.J. Bouchard, G.K. Dey, Mater. Sci. Eng. A 575 (2013) 160–168.

[14] G. Lu, D.W. Sokol, Y. Zhang, J.L. Dulaney, Appl. Mater. Today 15 (2019) 171–184.

[15] Y. Poitevin, P. Aubert, E. Diegele, G. de Dinechin, J. Rey, M. Rieth, E. Rigal, A. von der Weth, J.-L. Boutard, F. Tavassoli, J. Nucl. Mater. 417 (2011) 36–42.

[16] L.P. Jones, P. Aubert, V. Avilov, F. Coste, W. Daenner, T. Jokinen, K.R. Nightingale, M. Wykes, Fusion Eng. Des. 69 (2003) 215–220.

[17] Y.Q. Wang, M.W. Spindler, C.E. Truman, D.J. Smith, Mater. Des. 95 (2016) 656–668.

[18] Y.Q. Wang, H.E. Coules, C.E. Truman, D.J. Smith, Int. J. Solids Struct. 135 (2018) 219–232.

[19] J. Ahn, E. He, L. Chen, R.C. Wimpory, J.P. Dear, C.M. Davies, Mater. Des. 115 (2017) 441–457.

[20] P. Agrawal, S. Shukla, S. Gupta, P. Agrawal, R.S. Mishra, Appl. Mater. Today 21 (2020) 100853.

[21] D.G. Carr, M.I. Ripley, T.M. Holden, D.W. Brown, S.C. Vogel, Acta Mater. 52 (2004) 4083–4091.

[22] W. Woo, G.B. An, E.J. Kingston, A.T. Dewald, D.J. Smith, M.R. Hill, Acta Mater. 61 (2013) 3564–3574.

[23] W. Reimers, in: Structural and Residual Stress Analysis by Nondestructive Methods, Elsevier, 1997, pp. 461–494.

[24] R. Coppola, O. Asserin, P. Aubert, C. Braham, A. Monnier, M. Valli, E. Diegele, J. Nucl. Mater. 417 (2011) 51–54.

[25] R.S. Ramadhan, A.K. Syed, A.S. Tremsin, W. Kockelmann, R. Dalgliesh, B. Chen, D. Parfitt, M.E. Fitzpatrick, Mater. Des. 143 (2018) 56–64.

[26] C.M. Wensrich, J.N. Hendriks, A. Gregg, M.H. Meylan, V. Luzin, A.S. Tremsin, Nucl. Instrum. Methods Phys. Res. Sect. B Beam Interact. Mater. Atoms 383 (2016) 52–58.
[27] A.S. Tremsin, J.V. Vallerga, J.B. McPhate, O.H.W. Siegmund, R. Raffanti, IEEE Trans. Nucl. Sci. 60 (2013) 578–585.
[28] W. Kockelmann, T. Minniti, D.E. Pooley, G. Burca, R. Ramadhan, F.A. Akeroyd, G.D. Howells, C. Moreton-Smith, D.P. Keymer, J. Kelleher, S. Kabra, T.L. Lee, R. Ziesche, A. Reid, G. Vitucci, G. Gorini, D. Micieli, R.G. Agostino, V. Formoso, F. Aliotta, R. Ponterio, S. Trusso, G. Salvato, C. Vasi, F. Grazzi, K. Watanabe, J.W.L. Lee, A.S. Tremsin, J.B. McPhate, D. Nixon, N. Draper, W. Halcrow, J. Nightingale, J. Imaging 4 (2018) 4030047.
[29] H. Sato, T. Sato, Y. Shiota, T. Kamiyama, A.S. Tremsin, M. Ohnuma, Y. Kiyanagi, Mater. Trans. 56 (2015) 1147–1152.
[30] M. Busi, N. Kalentics, M. Morgano, S. Griffiths, A.S. Tremsin, T. Shinohara, R. Logé, C. Leinenbach, M. Strobl, Addit. Manuf. 39 (2021) 101848.
[31] Y. Su, K. Oikawa, T. Shinohara, T. Kai, T. Horino, O. Idohara, Y. Misaka, Y. Tomota, Sci. Rep. 11 (2021) 4155.
[32] M. Rieth, M. Schirra, A. Falkenstein, P. Graf, S. Heger, H. Kempe, R. Lindau, H. Zimmermann, EUROFER 97 Tensile, Charpy, Creep and Structural Tests, No. FZKA–6911, Forschungszentrum Karlsruhe GmbH Technik und Umwelt. Inst. fuer Materialforschung, Germany, 2003.
[33] F. Bachmann, R. Hielscher, H. Schaeben, Texture Analysis with MTEX – Free and Open Source Software Toolbox, Solid State Phenom. 160 (2010) 63–68.
[34] M.R. Daymond, M. Preuss, B. Clausen, Acta Mater. 55 (2007) 3089–3102.
[35] E. Oliver, J. Santisteban, J. James, M. Daymond, J. Dann, ENGIN-X user manual, ISIS. Rutherford-Appleton Laboratory, UK, 2004.
[36] R.B.V. Dreele, A.C. Larson, General Structure Analysis System (GSAS), Los. Alamos National Laboratory Report LAUR (2004) 86–748.
[37] M. Turski, S. Pratihar, L. Edwards, M.R. Daymond, M.E. Fitzpatrick, Mater. Sci. Forum 524–525 (2006) 677–684.
[38] G.S. Pawley, J. Appl. Crystallogr. 14 (1981) 357–361.
[39] T. Gnäupel-Herold, A.A. Creuziger, M. Iadicola, J. Appl. Crystallogr. 45 (2012) 197–206.
[40] T. Minniti, K. Watanabe, G. Burca, D.E. Pooley, W. Kockelmann, Nucl. Instrum. Methods Phys. Res. Sect. A Accel. Spectrom. Detect. Assoc. Equip. 888 (2018) 184–195.
[41] A.S. Tremsin, T.Y. Yau, W. Kockelmann, Strain 52 (2016) 548–558.
[42] C.A. Schneider, W.S. Rasband, K.W. Eliceiri, Nat. Methods 9 (2012) 671–675.
[43] J.R. Santisteban, L. Edwards, A. Steuwer, P.J. Withers, J. Appl. Crystallogr. 34 (2001) 289–297.
[44] A. Steuwer, P.J. Withers, J.R. Santisteban, L. Edwards, G. Bruno, M.E. Fitzpatrick, M.R. Daymond, M.W. Johnson, D. Wang, Phys. Status Solidi Appl. Res. 185 (2001) 221–230.
[45] E. Gaganidze, F. Gillemot, I. Szenthe, M. Gorley, M. Rieth, E. Diegele, Fusion Eng. Des. 135 (2018) 9–14.
[46] B. Roebuck, E.G. Bennett, A. Dickson, The measurement of uncertainty in grain size distribution. Interlaboratory exercise. Part 1 - Reference Images, Natl. Phys. Lab. CMMT(A)154 (1999).

[47] P. Staron, A. Schreyer, H. Clemens, S. Mayer, Neutrons and Synchrotron Radiation in Engineering Materials Science: From Fundamentals to Applications: Second Edition, John Wiley & Sons, 2017.
[48] W. Woo, V.T. Em, B.S. Seong, P. Mikula, G.B. An, J. Mater. Sci. 47 (2012) 5617–5623.
[49] Y.Q. Wang, S. Hossain, S. Kabra, S.Y. Zhang, D.J. Smith, C.E. Truman, J. Mater. Sci. 52 (2017) 7929–7936.
[50] B. Chen, J.N. Hu, Y.Q. Wang, S. Kabra, A.C.F. Cocks, D.J. Smith, P.E.J. Flewitt, J. Mater. Sci. 50 (2015) 5809–5816.
[51] N.S. Rossini, M. Dassisti, K.Y. Benyounis, A.G. Olabi, Mater. Des. 35 (2012) 572–588.
[52] H.H. Lai, W. Wu, J. Mater. Res. Technol. 9 (3) (2020) 2717–2726.
[53] L. Forest, N. Thomas, L. Cogneau, J. Tosi, J. Vallory, M. Zmitko, Y. Poitevin, M. Soldaini, G.A. Spagnuolo, C. Lacroix, M. Simon-Perret, Fusion Eng. Des. 164 (2021) 112210.
[54] J.S. Robinson, D.A. Tanner, S. Van Petegem, A. Evans, Mater. Sci. Technol. 28 (2012) 420–430.
[55] J. Moon, C.H. Lee, T.H. Lee, M.H. Jang, M.G. Park, H.N. Han, J. Nucl. Mater. 455 (2014) 81–85.
[56] W. Suder, S. Ganguly, S. Williams, A.M. Paradowska, P. Colegrove, Sci. Technol. Weld. Join. 16 (2011) 244–248.
[57] H. Sato, T. Kamiyama, Y. Kiyanagi, Mater. Trans. 52 (2011) 1294–1302.
[58] K. Iwase, H. Sato, S. Harjo, T. Kamiyama, T. Ito, S. Takata, K. Aizawa, Y. Kiyanagi, J. Appl. Crystallogr. 45 (2012) 113–118.
[59] G. Song, J. Lin, J. Bilheux, Q. Xie, L. Santodonato, J. Molaison, H. Skorpenske, A.M. Dos Santos, C. Tulk, K. An, A. Stoica, M. Kirka, R. Dehoff, A. Tremsin, J. Bunn, L. Sochalski-Kolbus, H. Bilheux, J. Imaging 3 (2017) 65.
[60] R. Dakhlaoui, V. Klosek, M.H. Mathon, B. Marini, Acta Mater. 58 (2010) 499–509.
[61] P.J. Withers, M. Preuss, A. Steuwer, J.W.L. Pang, J. Appl. Crystallogr. 40 (2007) 891–904.
[62] Z. Wang, E. Denlinger, P. Michaleris, A.D. Stoica, D. Ma, A.M. Beese, Mater. Des. 113 (2017) 169–177.
[63] D.J. Hughes, M.N. James, D.G. Hattingh, P.J. Webster, J. Neutron Res. 11 (2003) 289–293.
[64] E.O. Hall, Proc. Phys. Soc. Sect. B 64 (1951) 747.
[65] N.J. Petch, J. Iron Steel Inst. 174 (1953) 25–28.
[66] H. Bhadeshia, R. Honeycombe, Steels: Microstructure and Properties, Butterworth-Heinemann, 2017.
[67] T. Shrestha, I. Charit, G. Potirniche, J. Mater. Eng. Perform. 24 (2015) 4710–4720.
[68] Z.L. Hu, S.J. Yuan, X.S. Wang, G. Liu, H.J. Liu, Scr. Mater. 66 (2012) 427–430.
[69] Y.H. Lee, D. Kwon, Scr. Mater. 49 (2003) 459–465.
[70] J. Macchi, S. Gaudez, G. Geandier, J. Teixeira, S. Denis, F. Bonnet, S.Y.P. Allain, Mater. Sci. Eng. A 800 (2021) 140249.